

## Article

# The Analysis of the Compositional Uniformity of a Ti-Al Alloy during Electron Beam Cold Hearth Melting: A Numerical Study

Yunpeng Wang <sup>1</sup>, Yuchen Xin <sup>1</sup>, Lei Gao <sup>1,\*</sup> , Wei Cao <sup>2</sup>, Chong Ma <sup>2</sup>, Shenghui Guo <sup>1,\*</sup> and Guo Chen <sup>2</sup> 

<sup>1</sup> Faculty of Metallurgy and Energy Engineering, Kunming University of Science and Technology, Kunming 650093, China; wangypeng1997@163.com (Y.W.); mqxqqpvw@163.com (Y.X.)

<sup>2</sup> Key Laboratory of Green-Chemistry Materials in University of Yunnan Province, Yunnan Minzu University, Kunming 650500, China; caowei299@163.com (W.C.); mac89320@163.com (C.M.); guochen@kust.edu.cn (G.C.)

\* Correspondence: glkust2013@hotmail.com (L.G.); 20040051@kust.edu.cn (S.G.)

**Abstract:** The electron beam cold hearth melting (EBCHM) process is one of the key processes for titanium alloy production. However, EBCHM is prone to cause elemental volatilization and segregation during the melting of aluminum-containing titanium alloys such as Ti-6wt%Al-4wt%V. To gain deeper insights into the physical and chemical phenomena occurring during the EBCHM process, this paper establishes melting process models for the Ti-6wt%Al-4wt%V titanium alloy in a crystallizer with multiple overflow inlets. It examines the evolution of melt pool morphology, flow dynamics, heat transfer, and mass transfer during the casting process. The results indicate that the design of multi-overflow inlets can effectively suppress the longitudinal development of impact pits within the melt pool, thereby preventing the formation of solidification defects such as leaks in the melt. Concurrently, the diversion effect of multi-overflow inlets significantly enhances the elemental homogeneity within the melt pool. At a casting speed of 20 mm/min and a casting temperature of 2273 K, compared to a single overflow inlet, the design with three overflow inlets can reduce the depth of thermal impact pits within the crystallizer by 132 mm and decrease the maximum concentration difference in the Al element within the crystallizer by 0.933 wt.%. The aforementioned simulation results provide a theoretical basis for the control of metallurgical and solidification defects in large-scale titanium alloy ingots.



**Citation:** Wang, Y.; Xin, Y.; Gao, L.; Cao, W.; Ma, C.; Guo, S.; Chen, G. The Analysis of the Compositional Uniformity of a Ti-Al Alloy during Electron Beam Cold Hearth Melting: A Numerical Study. *Metals* **2024**, *14*, 884. <https://doi.org/10.3390/met14080884>

Academic Editor: Noé Cheung

Received: 20 June 2024

Revised: 25 July 2024

Accepted: 29 July 2024

Published: 31 July 2024



**Copyright:** © 2024 by the authors. Licensee MDPI, Basel, Switzerland. This article is an open access article distributed under the terms and conditions of the Creative Commons Attribution (CC BY) license (<https://creativecommons.org/licenses/by/4.0/>).

**Keywords:** electron beam cold hearth melting; numerical simulation; homogenization; Ti-6wt%Al-4wt%V

## 1. Introduction

Titanium and its alloys, such as Ti-6wt%Al-4wt%V, have low density, high tensile strength, and good toughness, which make them highly valuable and show their potential in aerospace, chemical, biomedical, and automotive lightweighting fields [1–5].

The traditional method for preparing the Ti-6wt%Al-4wt%V alloy is the VAR process, which has been challenged by the EBCHM process in the last decade [6–9]. The schematic diagram of the EBCHM is shown in Figure 1a, where the high-energy intensity electron beam is used as the heat source for melting feedstocks and maintaining the fluidity of molten alloy. Compared with VAR, the characteristic of EBCHM is that it introduces a cold hearth, which physically separates the melting, refining, and casting processes, and can more effectively remove the low-density inclusions (LDIs) formed by titanium and elements such as N, O, C, and the high-density inclusions (HDI) formed by elements such as W. Thus, the EBCHM process has a unique advantage in digesting titanium scraps [10], and effectively turns them into low-cost ultra-long titanium ingots (>10 m) [5]. In addition, EBCHM can flexibly change crystallizers with different sizes to produce slab ingots with different standards, thereby avoiding the forging and rolling processes required for VAR round ingots in the subsequent processing. This characteristic allows the iron and steel industries to participate in the rolling parts in the titanium production chain, using

the surplus steel rolling equipment to roll titanium ingots produced via EBCHM, thus promoting competitiveness in the metal production field [11–15].

However, high-quality titanium or titanium alloy ingots require delicate control during the EBCHM process under the high-temperature vacuum environment (above 1873 K, 0.001–0.1 Pa). It is necessary to control the physical environment around the melt and the corresponding solidification process, avoiding defects, including excessive inclusions (both LDIs and HDIs), surface checks, the heterogeneous distribution of elements, and so on, thus ensuring the composition and morphology of the final solidified microstructure [16–18]. The detailed ingot quality control techniques of EBCHM include controlling the residence time of titanium alloy in the cold hearth to eliminate and capture the inclusions; controlling the melt pool in the crystallizer to maintain a reasonable shape and depth to reduce the solidification defects during the casting process; and controlling the balance between the element loss and element replenishment during the melting process to ensure that no macro-segregation occurs in the ingot [19]. The above techniques are based on the rationality of the selection of raw materials, and melting process parameters (melting power, melting voltage, vacuum degree, cooling rate, etc.), which highly affect the interaction between heat transfer, flow, mass transfer, solidification, and other physical phenomena during the melting process. However, the melting environment inside the electron beam cold hearth furnace (high temperature, vacuum, metal mist, electron beam interference, etc.) is complex [20]. It is difficult to directly observe the physical phenomena during the melting process [21,22]. Therefore, the multi-physics coupling numerical model has become a key means to clarify the evolution law of physical phenomena during the electron beam cold hearth melting process [23,24].

Zhuk et al. established a steady-state numerical model of electron beam cold hearth melting of titanium alloy based on heat transfer and solidification theory, clarified the formation process of melt pool, and analyzed the correlation between the melting process window and melt pool depth [25]. In 2014, Zhao et al. used the finite volume method to establish a numerical model; studied the heat transfer, flow, and solidification process in Ti-6wt%Al-4wt%V titanium alloy melt pool under electron beam heating conditions; and simulated the formation process and influencing factors of melt pool morphology [26]. Klassen et al. established a numerical model for a small-scale electron beam additive manufacturing equipment, simulated the melting and volatilization process of Ti-6wt%Al-4wt%V titanium alloy under electron beam heating conditions, and studied the influence law of energy and mass transfer phenomena caused by volatilization on melt pool morphology evolution [27]. In 2017, this model further coupled with the mass transfer equation clarified the composition distribution and evolution law of Ti-48Al-2Cr-2Nb titanium alloy melt pool during the electron beam additive manufacturing process and provided a theoretical basis for the quality control of titanium alloy components during the additive manufacturing process [23]. Shuster et al. conducted a numerical simulation study on shrinkage porosity control during the electron beam cold hearth melting of a titanium alloy, proposed control conditions to reduce porosity volume, and provided an optimization scheme for the practical production process [28]. It can be seen that establishing a multi-physics coupling numerical model is a key process to reveal the physical phenomena and their evolution law in the melt pool during electron beam cold hearth melting of the Ti-6wt%Al-4wt%V titanium alloy. The simulation results are important for analyzing momentum transfer, heat transfer, and mass transfer phenomena during casting. They can provide a theoretical basis for clarifying the correlation between process parameters and defect formation and propose a quality control scheme for ingot.

In our previous work, we established a three-dimensional transient multi-physics coupling numerical simulation model to understand the evolution process of melt pool morphology in large-scale Ti-6wt%Al-4wt%V ingots (slab/round) during the melting process, flow state in the melt pool, and its influence law on the composition homogenization process [29–31].

For ingots with a small cross-sectional area, increasing the pulling speed during the melting process can form a melt pool stirring vortex zone along the longitudinal direction in the melt pool, effectively improving the homogenization efficiency of the melt body, and obtaining ingots with uniform chemical composition. However, there are still many unclear aspects in the existing research. It was found that increasing the casting and pulling speed did not significantly improve the chemical composition homogenization of large-scale slab ingots [32]. The main reason is that increasing the pulling speed will significantly increase the depth of the melt pit at the overflow inlet, limit the diffusion of the melt body outward, and easily cause leakage, affecting the solidification microstructure quality of the ingot.

In summary, to further understand the electron beam cold hearth process, this paper uses the verified three-dimensional transient multi-physics coupling numerical simulation model [29–31]. A numerical model is used to explore the casting process under a multi-overflow inlet design condition to reduce the possibility of leakage under a high flow rate in the crystallizer. The melting body is dispersed and poured into different positions of crystallizer, aiming to provide suggestions for the precise control of macro-segregation in a large-scale Ti-6wt%Al-4wt%V slab ingot EBCHM process.

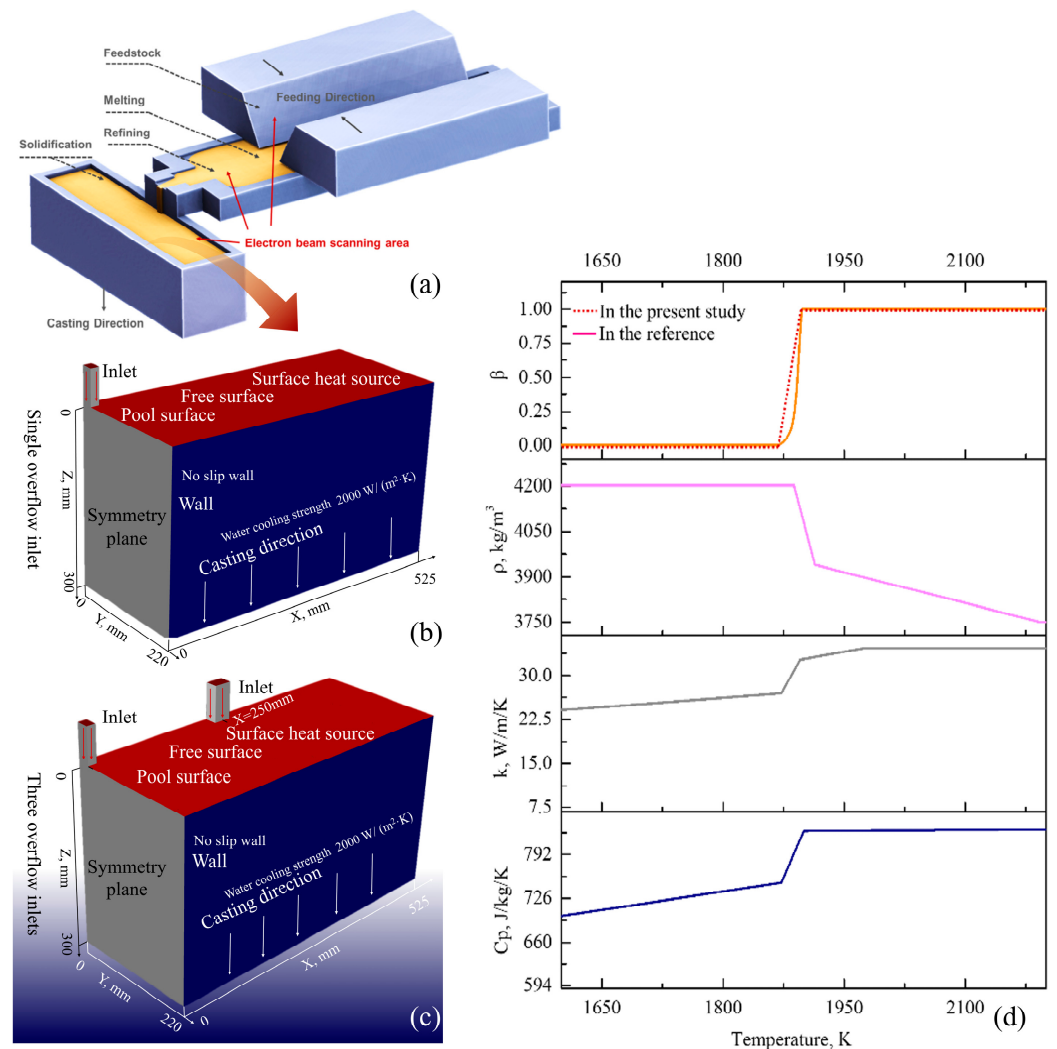


**Figure 1.** The schematic diagram of EBCHM (a); (b) single overflow inlet (Reproduced with permission from [31], published by Elsevier 2020); (c) three overflow inlets; (d) descriptions of physical properties of Ti-6wt%Al-4wt%V utilized in the present numerical model (adapted from [33]).

## 2. Model Description

The melting and casting process of EBCHM consists of three main phases: initial startup, steady-state operation, and make-up shrinkage phase. During the initial startup phase, a hydraulic arm pushes the feedstock from the feed system into the furnace chamber at a specific speed, where the feedstock is melted under the scanning heat of the electron beam. The molten titanium and titanium alloys flow through the refining cold hearth and into the water-cooled crystallizer area, which is equipped with ingot heads. Once the crystallizer is filled with melt, the ingot head begins to withdraw downwards, and after a certain period, the casting process transitions to a steady-state operation. During steady-state operation, the casting rate is controlled by the melting rate of the raw material. By maintaining a balance between the ingot pulling speed and the melting rate, a stable liquid bath is formed, the shape of which is determined by a combination of process parameters [34]. To further understand the physical and chemical phenomena that occur during the electron beam cold hearth melting process, this paper established the melting process models of the Ti-6wt%Al-4wt%V titanium alloy for the crystallizer (220 mm × 1050 mm) and studied the element loss control and homogenization behavior of the Ti-6wt%Al-4wt%V titanium alloy melt under high-temperature and high-vacuum conditions. In our previous research [29], we discovered that as long as the scanning frequency of the electron beam heat source is sufficiently high and the scanning gaps are sufficiently short, it can be considered a uniform surface heat source. Therefore, we assume the electron beam heat source to be a uniform surface heat source. The mathematical equations, design parameters, and boundary conditions based on the model are shown as follows.

### 2.1. Physical Phenomenon Model Equation

The physical phenomena in EBCHM mainly include metal melting and solidification, mass and heat transfer under flow influence, and continuous element volatilization on the melt pool surface. The numerical model established in this paper uses the solidification/melting model and the species transport model to calculate the solidification and mass transfer phenomena during the continuous casting process, respectively. The surface reaction is activated on the melt surface to study the influence of volatilization on the composition distribution of the melt pool and solidified part. A user-defined function programming model implements some specific parameter changes.

The equations involved are as follows:

Mass conservation

$$\frac{\partial \rho}{\partial t} + \nabla \cdot (\rho \vec{v}) = 0 \quad (1)$$

Since the volatilization of Ti and Al causes material loss, the conservation of total mass and surface mass does not exist, and the conservation of mass only exists in the interior of the melt.

Momentum conservation

$$\frac{\partial}{\partial t}(\rho \vec{v}) + \nabla \cdot (\rho \vec{v} \vec{v}) = -\nabla p + \nabla \cdot (\bar{\tau}) + \rho \vec{g} + \vec{S}_{i,p} + \vec{S}_{i,m} \quad (2)$$

where  $S_{i,p}$  is the thermosolutal buoyancy.

$$\frac{\partial}{\partial t}(\rho \vec{v}) + \nabla \cdot (\rho \vec{v} \vec{v}) = -\nabla p + \nabla \cdot (\bar{\tau}) + \rho \vec{g} + \vec{S}_{i,p} + \vec{S}_{i,m} \quad (3)$$

The momentum sink  $S_{i,m}$  in the mushy zone has the following form:

$$S_{i,m} = \frac{(1 - \beta)^2}{(\beta^3 + 0.01)} A_{mushy} (\vec{v} - \vec{v}_p) \quad (4)$$

where  $\beta$  is the liquid fraction,  $A_{mushy}$  is the mushy zone constant, and  $\vec{v}_p$  is the solid velocity owing to the casting speed. The name for solidification modeling is the enthalpy–porosity technique.

Energy equations

$$H = h + \Delta H = h_{ref} + \int_{T_{ref}}^T c_p dT + \beta \Delta H_f \quad (5)$$

$$\frac{\partial}{\partial t}(\rho H) + \nabla \cdot (\rho \vec{v} H) = \nabla \cdot (k \nabla T) + Q_r \quad (6)$$

where  $Q_r$  is reaction heat source term.

Species equations

To simulate the evaporation, mixing, and transport of aluminum during EBCHM, a convection-diffusion equation was added to predict the local mass fraction of each species,  $Y_{i,liq}$ , namely Al and Ti in the present case. This conservation equation has the following general form:

$$\begin{aligned} \frac{\partial}{\partial t}(\rho Y_{i,liq}) + \nabla \cdot (\rho [\beta \vec{v}_{liq} Y_{i,liq} + (1 - \beta) \vec{v}_p Y_{i,sol}]) \\ = R_i + \nabla \cdot (\rho \beta D_{i,m,liq} \nabla Y_{i,liq}) - K_i Y_{i,liq} \frac{\partial}{\partial t}(\rho(1 - \beta)) + \frac{\partial}{\partial t}(\rho(1 - \beta) Y_{i,liq}) \end{aligned} \quad (7)$$

where  $R_i$  is the net rate of the evaporation of species  $i$  via chemical reaction. An equation of this form will be solved for  $N = 1$  species, where  $N$  is the total number of fluid phase chemical species in the system. In the present study,  $N = 2$  because Al and Ti are mainly considered, and the evaporation of aluminum is assumed to be irreversible. The molar rate of the evaporation of Al ( $R_i$ ) can be calculated via the forward rate constant for the reaction  $k_{f,r}$  with data provided in Refs. [35,36] using the following equation:

$$R_i = k_{f,r} \left( \prod_{i=1}^{N_s} [C_i]_{suf}^{n'_{i,g,r}} \right) \left( \prod_{j=1}^{N_s} [S_j]_{suf}^{n'_{j,s,r}} \right) \quad (8)$$

$$k_{f,r} = A_r T^{\beta_r} e^{-E_r/RT} \quad (9)$$

The liquid ( $Y_{i,liq}$ ) and solid ( $Y_{i,sol}$ ) mass fractions are related to each other by the partition coefficient  $K_i$ :

$$Y_{i,sol} = K_i Y_{i,liq} \quad (10)$$

Supporting relations

The liquid fraction  $\beta$ , which is the fraction of the cell volume that is in the liquid form, is associated with each cell in the calculation domain based on the following equation:

$$\beta^{n+1} = \beta^n - \lambda \frac{a_p (T_c - T^*) \Delta t}{\rho V_c L_c - a_p \Delta t L_c \frac{\partial T^*}{\partial \beta}} \quad (11)$$

where the superscript  $n$  indicates the iteration number,  $\lambda$  is the relaxation factor with a default value of 0.9,  $a_p$  is the cell–matrix coefficient,  $\Delta t$  is the time step,  $\rho$  is the current density,  $V_c$  is the cell volume,  $L_c$  is the latent heat,  $T_c$  is the current cell temperature, and  $T^*$  is the interface temperature. In the current study, the Scheil rule model was used for species segregation at the micro-scale, and the corresponding  $T^*$  [35,36] was calculated by

$$T^* = T_{melt} + \sum_{i=0}^{N_t-1} m_i Y_i \beta^{K_i-1} \quad (12)$$

where  $T_{melt}$  is the melting temperature,  $N_t$  is the number of species,  $K_i$  is the partition coefficient of solute Al, and  $m_i$  is the slope of the liquidus surface.

## 2.2. Computational Domain and Boundary Conditions

The numerical simulation model involved in this paper is established using ANSYS Fluent 17.0 software. A half-symmetric geometric structure is selected as the computational domain to save computation time. The crystallizer design is for the casting demand of 220 mm × 1050 mm slab ingot, divided into two types in the present work: single-overflow-inlet-casting crystallizers and three-overflow-inlet-casting crystallizers, as shown in Figure 1b,c, along with the corresponding boundary conditions. The single-overflow-inlet-casting crystallizer is based on the actual equipment, and its corresponding geometric dimensions have been described in detail in our previous work (Figure 1b) [29–31]. The three-overflow-inlet crystallizer is a new design proposed for the first time in this article to divert the cold hearth melt (Figure 1c). According to the grid independence test, the computational domains described by a single overflow inlet and three overflow inlets consist of hexahedral grids for the overflow inlet and crystallizer.

The calculated parameter values used in the model computations are shown in Table 1. In the EBCHM process, the crystallizer has a water-cooling environment, and the corresponding heat transfer coefficient is taken as 2000 W/(m<sup>2</sup>·K) according to the literature suggestion [33]. The solute redistribution coefficient of elemental Al within Ti-6 wt%Al-4 wt%V during solidification is 1.167 [34]. We used FLUENT's Scheil rule model within the solid phase (assuming no diffusion within the solid phase). The liquid and solidus temperatures of Ti-6wt%Al-4wt%V are taken from the literature [33], which are 1928 K and 1878 K, respectively. The thermal conductivity  $k$ , specific heat  $C_p$ , liquid fraction  $\beta$ , and density  $\rho$  of Ti-6wt%Al-4wt%V are taken from the literature [33], and the results are shown in Figure 1d. The diffusivity of aluminum in molten Ti-6wt%Al-4wt%V was provided in reference [31]. Pressure–velocity coupling is used as the coupling algorithm; discrete model selection is PRESTO, based on Green–Gauss cell and third-order MUSCL.

**Table 1.** Calculated parameter values.

Name of Parameter	Value	References
Solute redistribution coefficient	1.167	[34]
Heat transfer coefficient	2000 W/(m <sup>2</sup> ·K)	[33]
Solid temperature	1928 K	[33]
Liquid temperature	1878 K	
Conductivity $k$	Figure 1d	
Specific heat $C_p$	Figure 1d	[33]
Liquid fraction $\beta$	Figure 1d	
Density $\rho$	Figure 1d	

## 2.3. Model Validation

The actual EBCHM of the Ti-6wt%Al-4wt%V titanium alloy takes a long time, and it is difficult to precisely control the pulling speed, temperature, and vacuum degree. However, due to the objective qualitative relationship between various parameters in the casting process, the collected data can be used to indirectly infer the accuracy of the model. Our previous work verified the accuracy of the numerical model established for predicting the physical and chemical processes in the crystallizer [29–31], in which the accuracy of the model for solidification process is verified according to the electron beam button experiments [33], as shown in Figure 2a, and the accuracy of the model for evaporation and mass transfer of the aluminum is verified as shown in Figure 2b, using the experiment data supported by the literature [37].

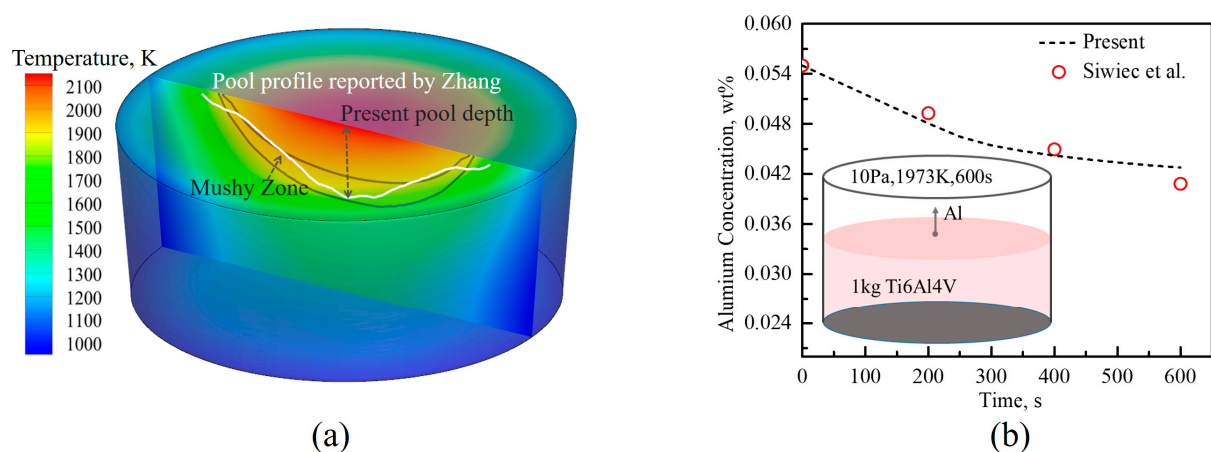


**Figure 2.** The accuracy of the model for solidification process is verified according to the electron beam button experiments adapted from [33] (a); the accuracy of the model for evaporation and mass transfer of the aluminum is verified using the experiment data supported by the literature adapted from Ref. [37] (b).

### 3. Results and Discussion

#### 3.1. Comparative Analysis of Al Element Homogenization between Single- and Three-Inlet Crystallizers in EBCHM

Our previous research has revealed the process of aluminum element segregation in the crystallizer by applying a single overflow inlet when casting 1050 mm × 220 mm Ti-6wt%Al-4wt%V slab ingot [30] (melting temperature of 2073–2273 K, pulling speed of 8–15 mm/min). Under the influence of a high melting temperature (2273 K) and relatively slow solute replenishment speed (8 mm/min), severe element segregation occurred at the boundary position of the ingot, which was challenging to meet the alloy configuration standard, as shown in Figure 3a. In our previous research, we tried to increase the solute replenishment speed by increasing the casting pulling speed from 8 mm/min to 15 mm/min, but the homogenization effect of the melt pool obtained was not ideal [30]. The main reason was that the thermal shock pit near the overflow inlet developed longitudinally, reducing mass transfer efficiency. The thermal shock pit is caused by the continuous replenishment of fluid energy at the overflow inlet during the solidification process of the ingot, and its depth is proportional to the casting speed. The melting body will form a vortex in the thermal shock pit, continuously consuming the overflow inlet's kinetic energy. Therefore, increasing casting speed has limited help in improving mass transfer efficiency, and it is challenging to suppress element segregation in the ingot effectively.

This paper further studies the improvement of homogenization conditions in crystallizer melt pool under a high pulling speed of 20 mm/min via the numerical simulation method, as shown in Figure 3b. This research results show that under this extremely high casting speed condition, the homogenization of cast ingot in crystallizer is significantly improved but at the cost of the rapid development of thermal shock deep pit at the overflow inlet, which increases from 0.049 m at 8 mm/min to 0.198 m at 20 mm/min, making it difficult for a large area near the overflow inlet to form a stable billet shell, which is prone to leakage, forming cold shuts, scabs, and other solidification defects. To explore possible methods to solve this problem, we tried to use a crystallizer applying three overflow inlets to divert the melt body, increase melt pool element replenishment while reducing thermal shock pit depth, reduce kinetic energy loss, and, thus, increase element homogenization efficiency in the melt pool. The melt pool cross-section, flow streamline mode, and aluminum content distribution obtained under a casting speed of 20 mm/min and casting temperature of 2273 K are shown in Figure 3c, and the thermal shock pit depth is 0.066 m.

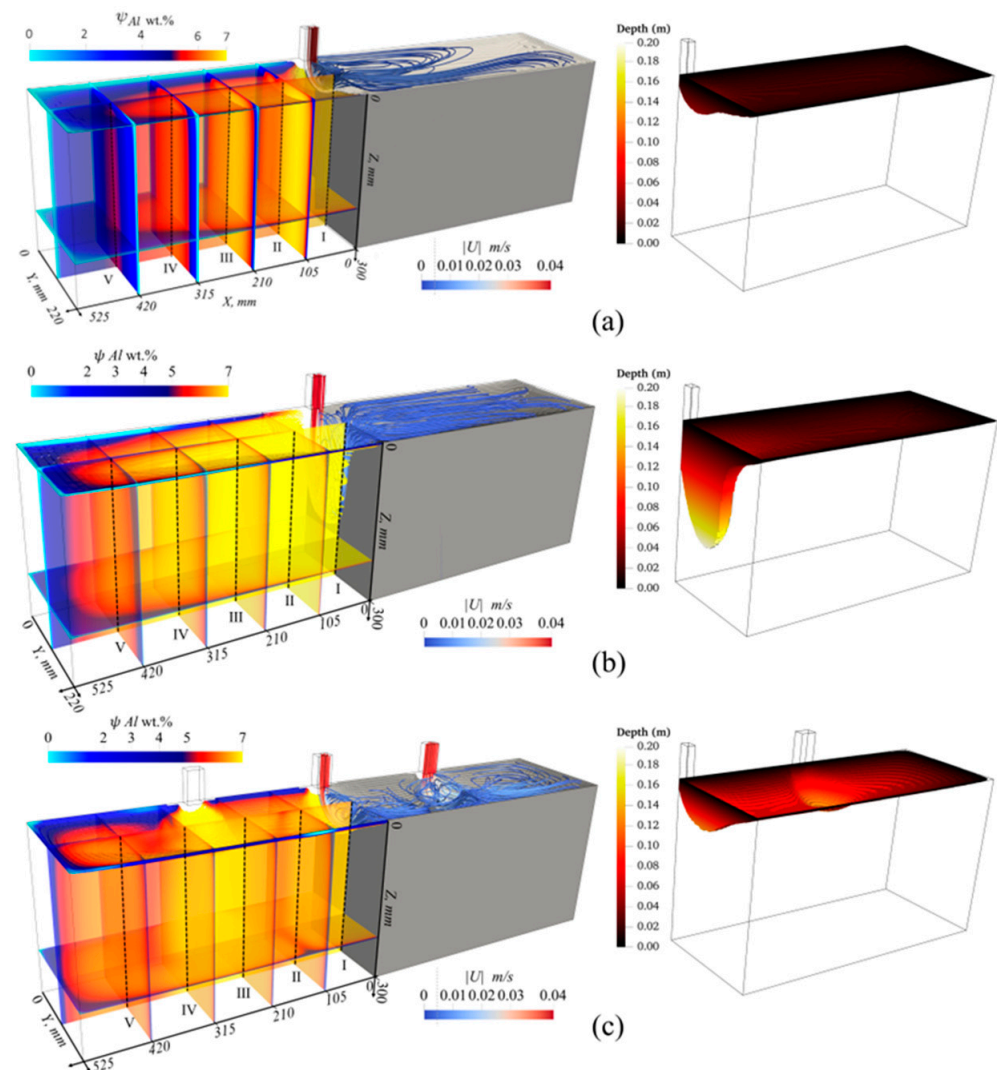


**Figure 3.** EBCHM numerical simulation presents the profile of the melt pool of the slab ingot with  $1050 \text{ mm} \times 220 \text{ mm}$ , along with flow streamline pattern and aluminum distribution at (a) 8 mm/min (single overflow inlet); (b) 20 mm/min (single overflow inlet); (c) 20 mm/min (three overflow inlets).

As shown in Figure 3c, three evenly distributed overflow inlets can make element replenishment in the melt pool more uniform and faster, fully solving the problem of uneven mass transfer and slow speed caused by one overflow inlet. At high pulling speeds, the thermal shock deep pit noticed in the pool was also restricted when overflow inlets increased.

We further analyzed the element segregation results to more quantitatively describe the difference between the two homogenization strategies. We took cross-sections at  $y = 110 \text{ mm}$  and  $x = 0, 105, 210, 315,$  and  $420 \text{ mm}$  in Figure 3b,c, respectively, and the corresponding changes in Al element concentration at their intersection are shown in Figure 4a,b. Due to less element evaporation, the Al element concentration increases continuously along the casting direction. In the solidification area, the maximum concentration difference in Al at the intersection of cross-sections is around 1 wt.%, as shown in Figure 4a, which is higher than the 0.643 wt.% obtained in the crystallizer melt pool using the design of three overflow inlets as shown in Figure 4b.

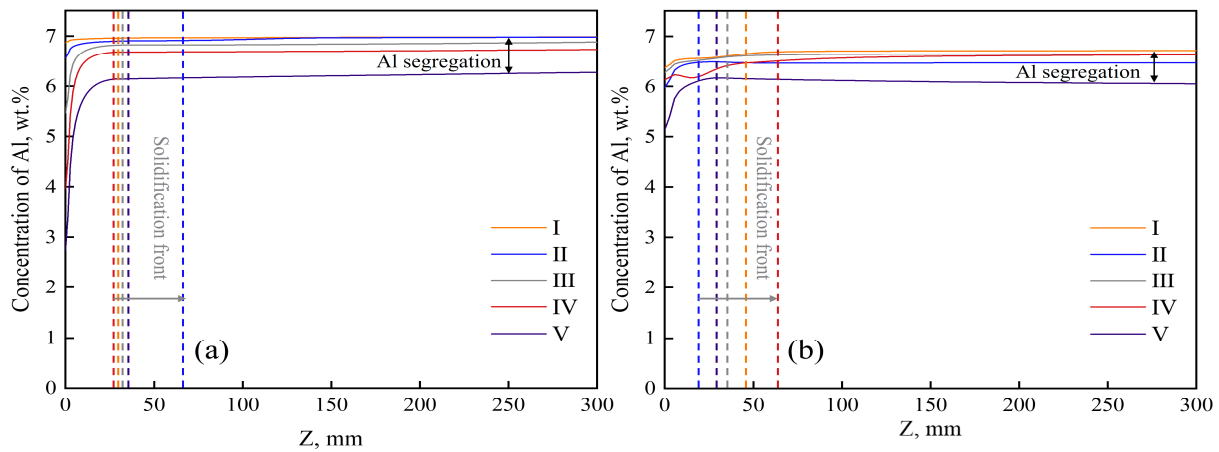


**Figure 4.** Al concentration at the intersection of  $y = 110$  mm slice and  $x = 0, 105, 210, 315,$  and  $420$  mm sections: (a) single overflow inlet; (b) three overflow inlets.

To evaluate the segregation degree on the melt pool and solidified cross-sections, we took point data of Al element concentration in the melt pool and on cross-sections in Figure 3b,c, respectively, and plotted the corresponding data of Al element concentration in descending order as shown in Figure 5a,b, respectively. In Figure 5a,b, the horizontal axis is the percentage of selected data in the dataset. For an ideal mixing pool, the slope of the plotting area should be close to zero. Conversely, a steep slope of the plotting area represents an insufficient mixing pool. Quantitatively, the segregation degree  $\Phi$  of extracted data is defined as the ratio of the sum of mixture concentration to the sum of initial concentration using Equation (13):

$$\Phi = \frac{\text{sum of mixture Al concentrations}}{\text{sum of initial Al concentrations}} \tag{13}$$

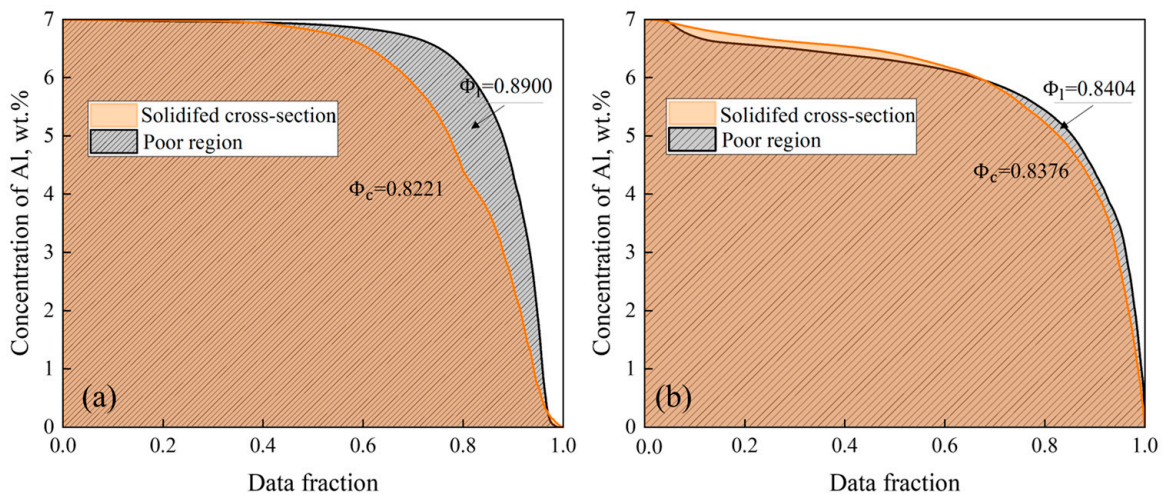


**Figure 5.** Al concentration in molten pool and solidification section; (a) single overflow inlet; (b) three overflow inlets.

Our findings indicate that the degree of segregation, determined by data extraction, results in  $\Phi_l$  and  $\Phi_c$  values of 0.8376 and 0.8404 within the melt pool and the solidification section, respectively. Compared to the melt pool in the single-overflow crystallizer, the slope change is more gradual, suggesting a more evenly balanced Al content within the melt pool, resulting in superior homogenization. A greater  $\Phi_l$  in the melt pool of the single overflow, the crystallizer can be attributed to the deeper overall depth of the melt, with less

renewal at the flanks. This reduces volatilization efficiency at the flank, causing a greater overall elemental loss than in the three overflow inlet crystallizers.

### 3.2. Influence of Pouring Temperature on Crystallizer in Three Overflow Inlets in EBCHM

To evaluate the influence of pouring temperature on the morphology of the melt pool and the degree of Al segregation, the EBCHM condition with a pulling speed of 20 mm/min was studied at respective temperatures of 2073 K, 2123 K, 2173 K, 2223 K, and 2273 K. The corresponding cross-sections of the melt pool are depicted in Figure 6a–e. Under the casting speed studied (20 mm/min), the pouring temperature has minor effects on the melt pool shape, with the maximum depth of the melt pool near the overflow position varying between 48 mm and 80 mm. More stable configured melt pools favor the grain refinement of the ingot, as they permit the formation of dendritic structures parallel to the chunk axis [38]. The corresponding average velocity ( $\bar{u}$ ) within the pool ranged from 4.64 mm/s to 6.58 mm/s. Using the Reynolds number to distinguish between laminar and turbulent flows, the evolution of the flow state in the x-direction,  $Re$ , is presented in Figure 6f, calculated using the following equation [39]:

$$Re = \rho u L / \quad (14)$$

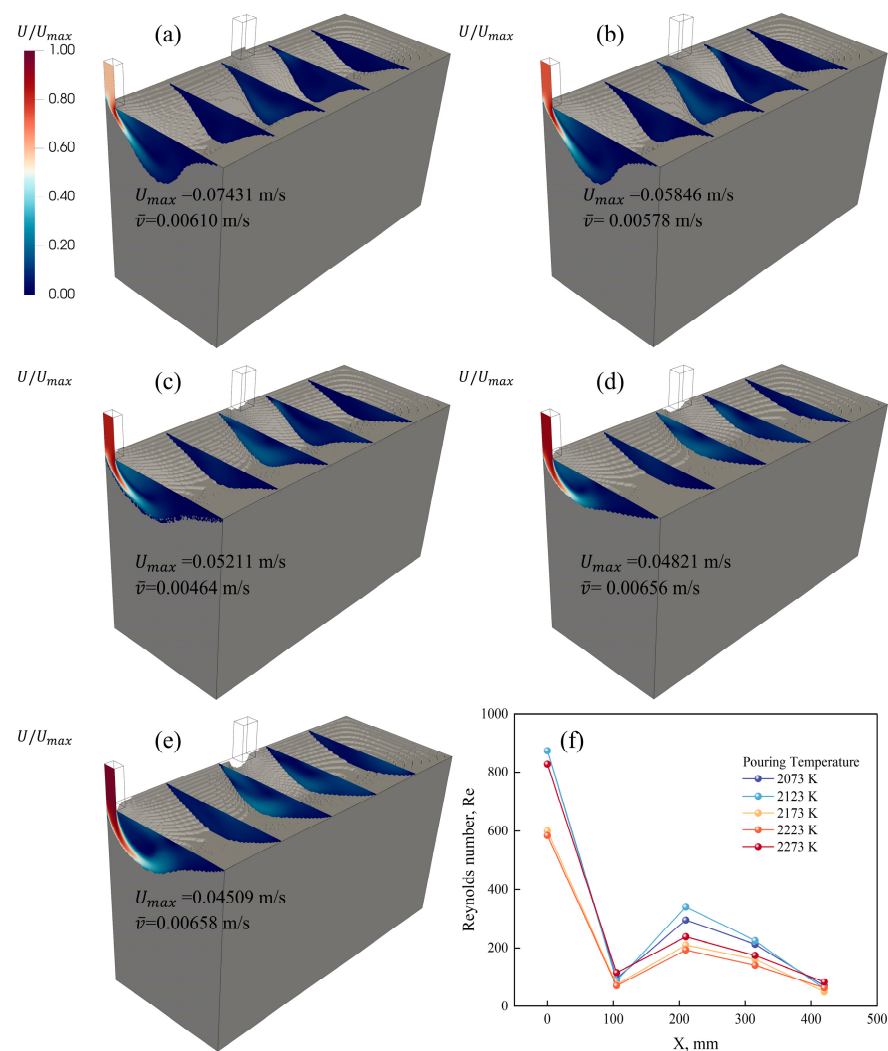


**Figure 6.** Under the conditions of pouring temperatures of (a) 2073 K, (b) 2123 K, (c) 2173 K, (d) 2223 K, and (e) 2273 K, and a casting speed of 20 mm/min, EBCHM obtained the normalized velocity distributions in the y-z plane for a series of equally spaced slices at  $x = 0, 105, 210, 315,$  and  $420$  mm; (f) the average Reynolds number on the slices in the pool.

Among them,  $\rho$  is the density ( $\text{kg/m}^3$ ),  $u$  is the velocity ( $\text{m/s}$ ),  $L$  is the characteristic length ( $\text{m}$ ), and  $\mu$  is the dynamic viscosity ( $\text{Pa}\cdot\text{s}$ ). The flow state in the pool is laminar flow; because the  $Re$  decreases along the  $x$  direction, the maximum  $Re$  value is below 900. Therefore, the effect of turbulent diffusion on the results of the aluminum transport equation can be ignored.

Figure 7a illustrates the positions of the cross-sections in the mold at  $x = 0$  mm,  $x = 250$  mm, and  $x = 500$  mm. Figure 7b presents the melt pool depths at these positions under various temperatures. The cross-section at  $x = 0$  mm corresponds to the red melt pool, the cross-section at  $x = 250$  mm corresponds to the green melt pool, and the cross-section at  $x = 500$  mm corresponds to the blue melt pool. The overflow ports at  $x = 0$  mm and  $x = 250$  mm are located on the same side, resulting in nearly overlapping melt pool profiles for these positions. At a casting temperature of 2073 K, the maximum melt pool depth is 77.5 mm; when the casting temperature increases to 2223 K, the melt pool depth significantly decreases, with a minimum depth of 47.9 mm. In contrast, the melt pool at  $x = 500$  mm, situated on the opposite side of the overflow port, shows minimal depth variation with different casting temperatures, maintaining relatively stable depths across temperatures.

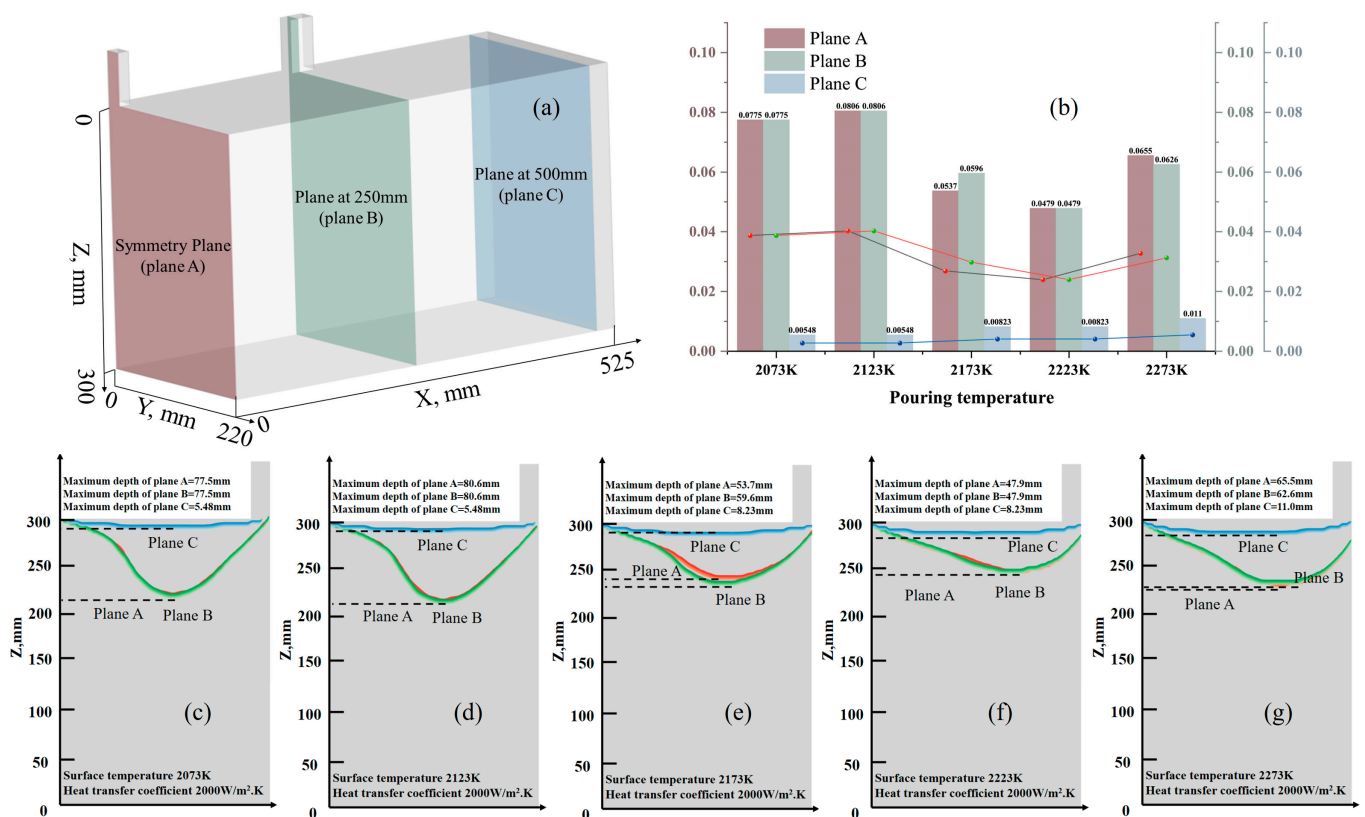


**Figure 7.** (a) Schematic of melt pool cross-sections at  $x = 0$ , 250, and 500 mm within the mold. (b) Bar chart of melt pool depths at a casting speed of 20 mm/min and casting temperatures of 2073 K, 2123 K, 2173 K, and 2223 K. Melt pool profiles at a casting speed of 20 mm/min and casting temperatures of (c) 2073 K, (d) 2123 K, (e) 2173 K, (f) 2223 K, and (g) 2173 K for the three cross-section positions.

In summary, the melt pool depths at  $x = 0$  mm and  $x = 250$  mm, on the same side as the overflow port, vary significantly with casting temperature. However, at  $x = 500$  mm on the opposite side, the depths remain relatively constant. This indicates that the position of the overflow port and the casting temperature are critical factors affecting the melt pool depth.

The distribution of Al within the melt pool under different casting temperatures is shown in Figure 8a–e. The average concentration in the melt pool decreases as the casting temperature increases. Specifically, when the ingot temperatures are 2073 K, 2123 K, 2173 K, 2223 K, and 2273 K, the average Al concentrations within the melt pool are 6.88%, 6.77%,

6.52%, 6.32%, and 5.88%, respectively. The corresponding standard deviations of the Al concentrations are 0.13, 0.28, 0.62, 0.77, and 1.13. The data distribution of Al in the melt pool at different temperatures, based on nodal data within the melt pool region, is depicted in Figure 8f. The results show that the corresponding segregation degree  $\Phi_l$  at casting temperatures of 2073 K, 2123 K, 2173 K, 2223 K, and 2273 K are 0.98, 0.97, 0.93, 0.90, and 0.84, respectively.

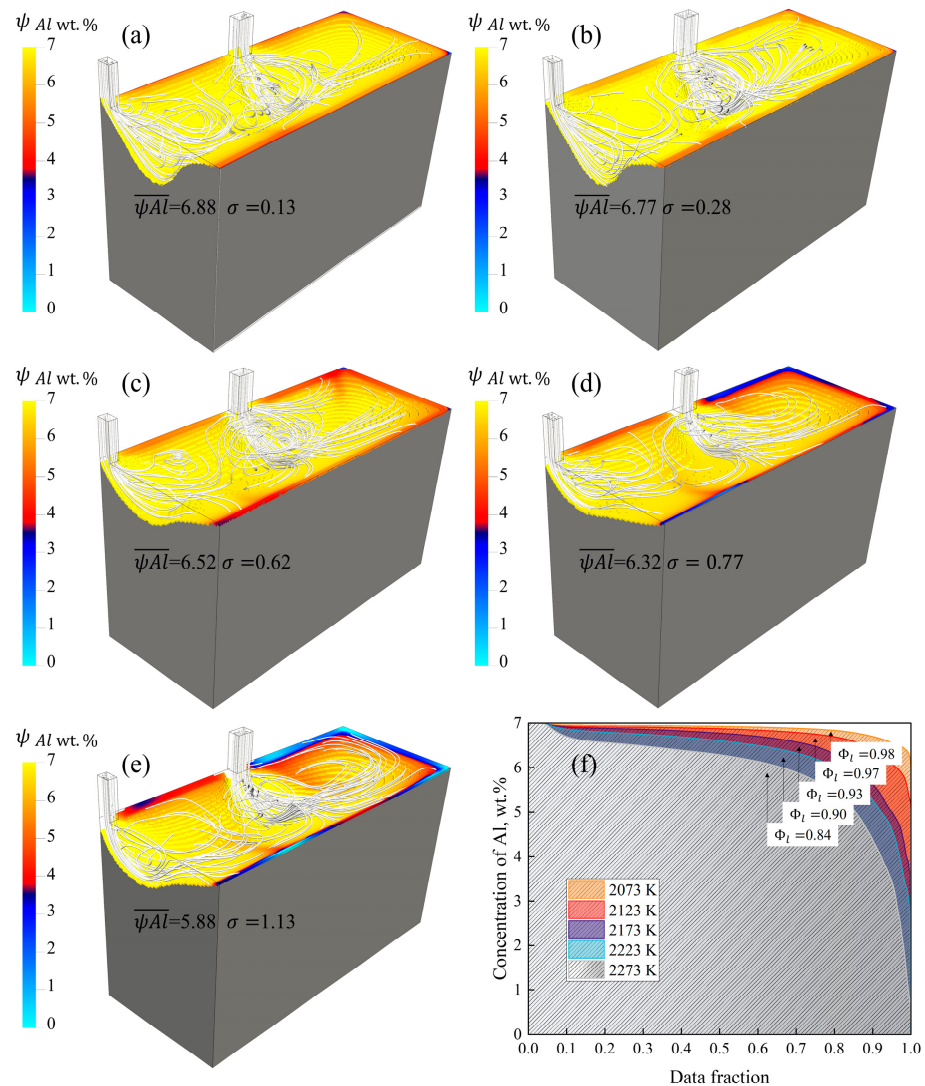


**Figure 8.** Distribution of aluminum concentration in the molten pool of ingot at temperatures of (a) 2073 K, (b) 2123 K, (c) 2173 K, (d) 2223 K, and (e) 2273K; casting speed of 20 mm/min; (f) change in Al segregation degree  $\Phi_l$  in molten pool with pouring temperature.

Figure 9a–e present the distribution of Al in the solidification section when the ingot temperatures are 2073 K, 2123 K, 2173 K, 2223 K, and 2273 K with a pulling speed of 20 mm/min. The corresponding average Al concentrations are 6.80%, 6.68%, 6.47%, 6.22%, and 5.86%, with standard deviations of 0.28, 0.43, 0.70, 0.96, and 1.33, respectively. Based on the data from this section, the data distribution of Al concentration in the solidification section is shown in Figure 9f. The corresponding segregation degrees of  $\Phi_c$  are 0.97, 0.95, 0.92, 0.89, and 0.83, respectively.

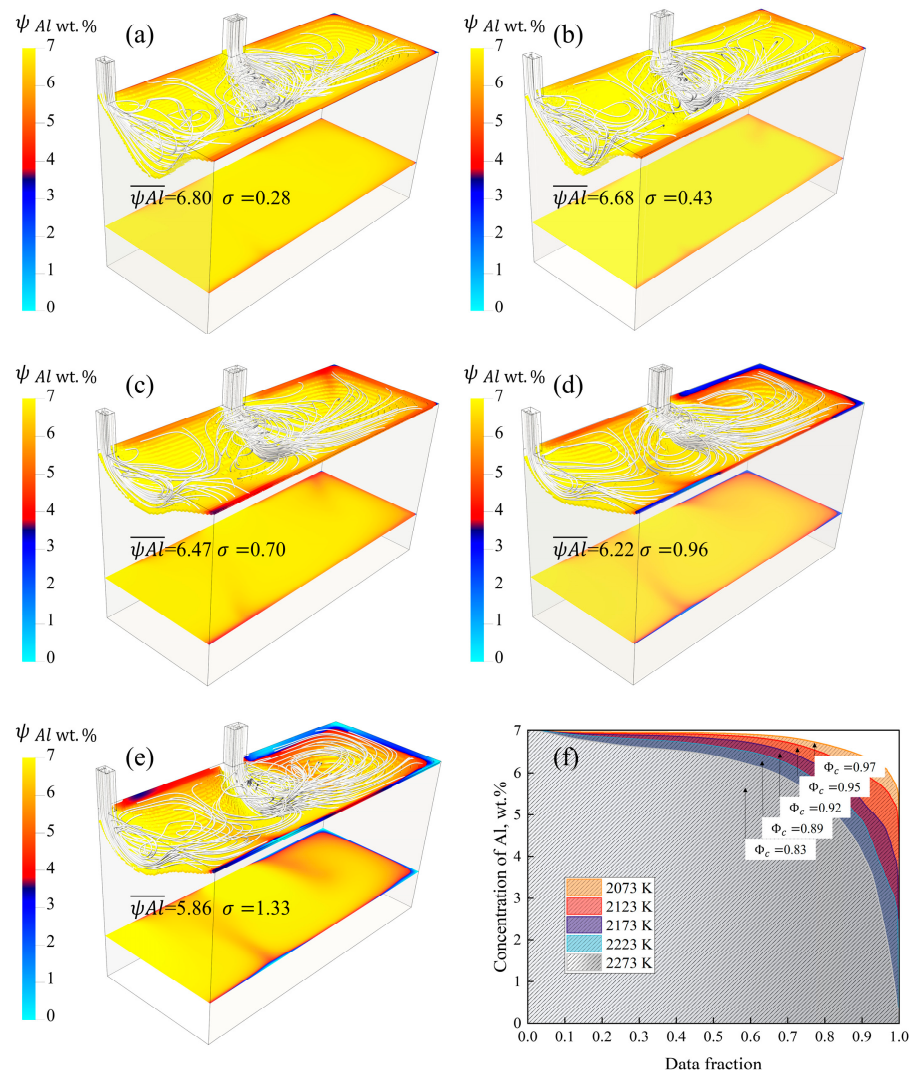


**Figure 9.** Distribution of aluminum on solidification cross-section ( $Z = 220$  mm) of ingot at (a) 2073 K, (b) 2123 K, (c) 2173 K, (d) 2223 K, and (e) 2273 K, with a casting speed of 20 mm/min; (f) change in Al segregation degree  $\Phi_c$  on the solidification section with pouring temperature.

The discussions above show that macro-segregation within EBCHM ingots can be effectively managed through appropriate casting conditions. As shown in Table 2, within the temperature range of 2073–2273 K, the elemental segregation in the melt pool and the final ingot is kept above 0.8. The primary segregation locations of the elements are confined to the peripheries of the ingot. Subsequent surface peeling operations should further enhance the quality of the ingot.

**Table 2.** The segregation degrees in the EBCHM ingots with different casting conditions.

Pouring Temperature (K)	$\Phi_l$	$\Phi_c$
2073	0.9826	0.9717
2123	0.9667	0.9539
2173	0.9312	0.9238
2223	0.9029	0.8888
2273	0.8404	0.8376

#### 4. Conclusions

The electron beam cold hearth melting (EBCHM) process is vital in titanium alloy production, improving ingot quality and casting efficiency. To better understand the physical and chemical phenomena in the EBCHM process, we modeled the Ti-6wt%Al-4wt%V titanium alloy melting process for a 220 mm × 1050 mm crystallizer. The study examines the casting process with a multi-overflow-inlet design to reduce leakage risk at high flow rates compared to a single-overflow-inlet crystallizer. These models investigate solidification, flow, heat transfer, and mass transfer in the melt pool during casting. The key conclusions include the following:

- (1) The crystallizer with three overflow inlets, at a casting speed of 20 mm/min and ingot temperatures from 2073 K to 2273 K, resulted in a thermal impact pit depth of 48–80 mm. Average Reynolds numbers at five cross-sections were 310, 317, 219, 210, and 288, respectively. Compared to a single inlet, this design reduced pit depth by 132 mm, improving solidification quality under high temperatures and speeds.
- (2) As the temperature decreased from 2273 K to 2073 K, Al segregation in the three-overflow-inlet crystallizer increased from 0.84 to 0.98 in the melt pool and from 0.84 to 0.97 in the solidification cross-section. Compared to a single inlet, the maximum Al concentration difference decreased by 0.933 wt.%, showing that multiple overflow inlets improve homogenization and reduce segregation.

**Author Contributions:** Conceptualization, L.G. and S.G.; methodology, L.G. and Y.W.; software, Y.X. and Y.W.; validation, L.G. and Y.W.; formal analysis, W.C. and C.M.; investigation, L.G.; resources, L.G., S.G. and G.C.; data curation, Y.X., W.C. and C.M.; writing—original draft preparation, Y.W., W.C. and C.M.; writing—review and editing, L.G., G.C. and S.G.; visualization, Y.W.; supervision, G.C. and S.G.; project administration, Y.W.; funding acquisition, L.G. and S.G. All authors have read and agreed to the published version of the manuscript.

**Funding:** This research was funded by the National Natural Science Foundation of China under grant number 52104351, the Technology Major Project of Yunnan Province under grant number 202202AG050007, and Yunnan Fundamental Research Projects under grant number 202301AT070795, 202101AU070088, and the authors (L.G., S.G. and G.C.) would like to acknowledge the Yunnan Province Xingdian Talent Support Plan Project.

**Data Availability Statement:** The original contributions presented in the study are included in the article, further inquiries can be directed to the corresponding author.

**Acknowledgments:** Thanks for the great effort of the editors and reviewers.

**Conflicts of Interest:** The authors declare no conflicts of interest.

#### Nomenclature

$\beta$	liquid fraction
$\beta_{c,i}$	concentration expansion coefficient of component $i$ , 1/wt.%
$\beta_T$	thermal expansion coefficient, 1/K
$\lambda$	relaxation factor with a default value
$T_c$	cell temperature, K
$T^*$	interface temperature, K
$\rho$	density, kg/m <sup>3</sup>
$V_c$	cell volume, m <sup>3</sup>
$L_c$	latent heat of the material, J/kg
$a_p$	cell–matrix coefficient
$\Delta t$	time-step, s
$T_{melt}$	melting temperature, K
$N_s$	number of species
$m_i$	the slope of the liquidus surface with respect to $Y_i$
$Y_i$	the mass fraction of solute $i$

$K_i$	the partition coefficient of solute $i$
$S_1$	the momentum sink
$\varepsilon_c$	a small number (0.001) to prevent division by zero
$A_{mush}$	mushy zone constant
$\vec{v}$	cell velocity, m/s
$\vec{v}_p$	pull velocity, m/s
$T_{liq}$	liquidus temperature of the material, K
$T$	temperature, K
$Q_r$	reaction heat source term, W/m <sup>3</sup>
$R$	universal gas constant, J/mol K
$R_i$	reaction rate, kg/m <sup>2</sup> s
$\vec{v}_{liq}$	velocity of the liquid, m/s
$D_{i,m,liq}$	mass diffusion coefficient for species in the mixture, m <sup>2</sup> /s
$k_{f,r}$	forward rate constant for reaction $r$
$N_g$	number of gaseous species
$[C_i]_{suf}$	molar concentrations of gaseous species
$[S_i]_{suf}$	molar concentrations of site species
$\eta'_{i,g,r}$ and $\eta'_{i,s,r}$	the rate exponents for the $i$ th gaseous species as reactant and product, respectively
$\eta_{j,g,r}$ and $\eta_{j,s,r}$	the rate exponents for the $j$ th gaseous species as reactant and product, respectively
$A_r$	pre-exponential factor (consistent units)
$\beta_r$	temperature exponent (dimensionless)
$E_r$	activation energy for the reaction, J/mol
$\mu$	dynamic viscosity, Pa·s
$u$	velocity of the fluid with respect to the object, m/s
$L$	characteristic length, m
$Re$	Reynolds number

## References

- Gomez-Gallegos, A.; Mandal, P.; Gonzalez, D.; Zuelli, N.; Blackwell, P. Studies on titanium alloys for aerospace application. In *Defect and Diffusion Forum*; Trans Tech Publications Ltd.: Stafa-Zurich, Switzerland, 2018; Volume 385, pp. 419–423. [\[CrossRef\]](#)
- Qiu, G.; Guo, Y. Current situation and development trend of titanium metal industry in China. *Int. J. Miner. Metall. Mater.* **2022**, *29*, 599–610. [\[CrossRef\]](#)
- Wang, Y.P.; Tan, F.G.; Gao, L.X.; Zhou, L.; Shi, Z.; Li, N. Numerical Simulation Study on the Effects of Co-Injection of Pulverized Coal and SPL (Spent Pot-Lining) into the Blast Furnace. *Fuel* **2023**, *354*, 129368. [\[CrossRef\]](#)
- Zheng, H.W.; Hao, X.D.; Zhang, S.R.; Omran, M.; Chen, G.; Chen, J.; Gao, L. Modeling of process and analysis of drying characteristics for natural TiO<sub>2</sub> under microwave heating. *Chem. Eng. Process.-Process Intensif.* **2022**, *174*, 108900. [\[CrossRef\]](#)
- Chen, J.; Guo, S.H.; Omran, M.; Gao, L.; Zheng, H.W.; Chen, G. Microwave-assisted preparation of nanocluster rutile TiO<sub>2</sub> from titanium slag by NaOH-KOH mixture activation. *Adv. Powder Technol.* **2022**, *33*, 103549. [\[CrossRef\]](#)
- Jiang, D.; Ren, Y.; Zhang, L. Numerical Simulation of Inclusion Distribution in Vacuum Arc Remelting Ingot. *Metall. Mater. Trans. B* **2023**, *54*, 1342–1351. [\[CrossRef\]](#)
- Ji, S.; Duan, J.; Yao, L.; Maijer, D.M.; Cockcroft, S.L.; Fiore, D.; Tripp, D.W. Quantification of the heat transfer during the plasma arc re-melting of titanium alloys. *Int. J. Heat Mass Transf.* **2018**, *119*, 271–281. [\[CrossRef\]](#)
- Yu, J.X.; Yuan, Q.Q.; Huang, H.G.; Huang, Z.R.; Zhang, H.Y.; Wang, J.S.; Liu, K.; Yu, K.; Xiao, H. Influence of Annealing Treatment on  $\alpha$  Phase Globularization, Mechanical Properties, and Corrosion Performance of Hot-Rolled Ti–0.3Mo–0.8Ni Alloy Melted by Electron Beam Cold Hearth Technology. *Met. Mater. Trans. A* **2023**, *54*, 2872–2889. [\[CrossRef\]](#)
- Yu, J.X.; Yin, Z.P.; Huang, Z.R.; Zhao, S.; Huang, H.G.; Yu, K.; Zhou, R.F.; Xiao, H. Effect of aging treatment on microstructural evolution and mechanical properties of the electron beam cold hearth melting Ti-6Al-4V alloy. *Materials* **2022**, *15*, 7122. [\[CrossRef\]](#) [\[PubMed\]](#)
- Cen, M.J.; Liu, Y.; Chen, X.; Zhang, H.W.; Li, Y.X. Inclusions in melting process of titanium and titanium alloys. *China Foundry* **2019**, *16*, 223–231. [\[CrossRef\]](#)
- Peng, B.B.; Li, X.M.; Wang, X.; Mo, J.; Luo, L. Simulation study on temperature field and microstructure of Ti-6Al-4V alloy round ingot during EBCHM. *Mater. Res. Express* **2021**, *8*, 046505. [\[CrossRef\]](#)
- Wang, X.; Liu, Q.L.; Li, X.M. Effect of crystallize's three-dimension on the solid-liquid interface morphology of the large-scale Ti64 during EBCHM. *Mater. Res. Express* **2019**, *6*, 0865h4. [\[CrossRef\]](#)
- Zhang, H.Z.; Yi, J.H.; Wang, J.S.; Xiao, H.; Wang, M.; Wang, W. Effect of Direct Rolling Process on Microstructure and Mechanical Properties of the Electron Beam Cold Hearth Melting Ti-6Al-4V Alloy. *Metals* **2022**, *12*, 2018. [\[CrossRef\]](#)

14. Zhu, Z.Z.; Li, Z.L.; Zhou, R.F.; Huang, H.G.; Xiong, W.T.; Li, X.M. Experimental verification of molybdenum segregation for large-scale slab ingots of Ti–0.3 Mo–0.8 Ni alloy during electron-beam cold-hearth melting. *Philos. Mag. Lett.* **2022**, *102*, 270–277. [CrossRef]
15. Markovsky, P.E.; Bondarchuk, V.I.; Akhonin, S.V.; Berezos, A.V. Electron beam cold hearth melted titanium alloys and the possibility of their use as anti-ballistic materials. *MATEC Web Conf.* **2020**, *321*, 11036. [CrossRef]
16. Casem, D.T.; Weerasooriya, T.; Walter, T.R. Mechanical behavior of a low-cost Ti–6Al–4V alloy. *J. Dyn. Behav. Mater.* **2018**, *4*, 138–149. [CrossRef]
17. Liu, Q.L.; Jiang, Y.H.; Li, X.M. The effect of bulk nucleation parameters on the formation of macroscopic grain of the large-scale titanium slab ingot during EBCHM. *Mater. Sci. Technol.* **2018**, *34*, 1649–1656. [CrossRef]
18. Liu, R.; Hui, S.X.; Ye, W.J.; Yu, Y.; Fu, Y.Y.; Song, X.Y. Dynamic Compression Properties of Low-Cost Ti–6Al–4V Plates. In *Materials Science Forum*; Trans Tech Publications Ltd.: Stafa-Zurich, Switzerland, 2016; Volume 849, pp. 276–280. [CrossRef]
19. Truong, V.D.; Hyun, Y.T.; Won, J.W.; Lee, W.; Yoon, J. Numerical simulation of the effects of scanning strategies on the aluminum evaporation of titanium alloy in the electron beam cold hearth melting process. *Materials* **2022**, *15*, 820. [CrossRef] [PubMed]
20. Ivanchenko, V.G.; Ivasishin, O.M.; Semiatin, S.L. Evaluation of evaporation losses during electron-beam melting of Ti–Al–V alloys. *Metall. Mater. Trans. B* **2003**, *34*, 911–915. [CrossRef]
21. Markov, M.; Stefanova, V.; Vutova, K. The effectiveness of electron beam melting for removing impurities from technogenic metal materials. *J. Chem. Technol. Metall.* **2024**, *59*, 419–430. [CrossRef]
22. Ward, R.; Blenkinsop, B.; Evans, E.; Flower, F. Temperature sensing for cold hearth melting process. In *Titanium Science & Technology*; Springer: Berlin/Heidelberg, Germany, 1995; pp. 1478–1485.
23. Klassen, A.; Forster, V.E.; Juechter, V.; Körner, C. Numerical simulation of multi-component evaporation during selective electron beam melting of TiAl. *J. Mater. Process Technol.* **2017**, *247*, 280–288. [CrossRef]
24. Liu, Q.L.; Li, X.M.; Jiang, Y.H. Microstructure evolution of large-scale titanium slab ingot based on CAFE method during EBCHM. *J. Mater. Res.* **2017**, *32*, 3175–3182. [CrossRef]
25. Zhuk, H.V.; Kobryn, P.A.; Semiatin, S.L. Influence of heating and solidification conditions on the structure and surface quality of electron-beam melted Ti–6Al–4V ingots. *J. Mater. Process Technol.* **2007**, *190*, 387–392. [CrossRef]
26. Zhao, X.; Reilly, C.; Yao, L.; Maijer, D.M.; Cockcroft, S.L.; Zhu, J. A three-dimensional steady state thermal fluid model of jumbo ingot casting during electron beam re-melting of Ti–6Al–4V. *Appl. Math. Model.* **2014**, *38*, 3607–3623. [CrossRef]
27. Klassen, A.; Scharowsky, T.; Körner, C. Evaporation model for beam based additive manufacturing using free surface lattice Boltzmann methods. *J. Phys. D Appl. Phys.* **2014**, *47*, 275303. [CrossRef]
28. Shuster, R.E. Modeling of Aluminum Evaporation during Electron Beam Cold Hearth Melting of Titanium Alloy Ingots. Ph.D. Thesis, University of British Columbia, Vancouver, BC, Canada, 2013. [CrossRef]
29. Gao, L.; Huang, H.G.; Zhang, Y.Q.; Zhang, H.M.; Shi, Z.; Jiang, Y.H.; Zhou, R. Numerical modeling of EBCHM for large-scale Ti–6WT%AL–4WT%V alloy round ingots. *JOM* **2018**, *70*, 2934–2942. [CrossRef]
30. Gao, L.; Li, X.M.; Huang, H.G.; Sui, Y.D.; Zhang, H.M.; Shi, Z.; Chattopadhyay, K.; Jiang, Y.H.; Zhou, R. Numerical study of aluminum segregation during electron beam cold hearth remelting for large-scale Ti–6 wt% Al–4 wt% V alloy round ingot. *International. J. Heat Mass Transf.* **2019**, *139*, 764–772. [CrossRef]
31. Gao, L.; Huang, H.G.; Kratzsch, C.; Zhang, H.M.; Chattopadhyay, K.; Jiang, Y.H.; Zhou, R. Numerical study of aluminum segregation during electron beam cold hearth melting for large-scale Ti–6 wt% Al–4 wt% V alloy slab ingots. *International. J. Heat Mass Transf.* **2020**, *147*, 118976. [CrossRef]
32. Wang, Y.P.; Gao, L.; Xin, Y.C.; Guo, S.H.; Yang, L.; Ji, H.H.; Chen, G. Numerical Modeling of Electron Beam Cold Hearth Melting for the Cold Hearth. *Minerals* **2024**, *14*, 601. [CrossRef]
33. Zhang, Z.K. Modeling of Al Evaporation and Marangoni Flow in Electron Beam Button Melting of Ti–6Al–4V. Master’s Thesis, University of British Columbia, Vancouver, BC, Canada, 2013. [CrossRef]
34. Wu, S.; Liu, D.; Su, Y.; Guo, E.J.; Zhang, Y.H. Modeling of microstructure formation of Ti–6Al–4V alloy in a cold crucible under electromagnetic field. *J. Alloys Compd.* **2008**, *456*, 85–95. [CrossRef]
35. Chen, H.B.; Long, M.J.; Chen, D.F.; Liu, T.; Duan, H.M. Numerical study on the characteristics of solute distribution and the formation of centerline segregation in continuous casting (CC) slab. *Int. J. Heat Mass Transf.* **2018**, *126*, 843–853. [CrossRef]
36. ANSYS Inc. *ANSYS Fluent Theory Guide, Release 15.0*; ANSYS Inc.: Canonsburg, PA, USA, 2013.
37. Siwec, G.; Mizera, J.; Jama, D.; Szmaj, A.; Burdzik, R. The effects of temperature on the kinetics of aluminium evaporation from the Ti–6Al–4V alloy. *Metalurgija* **2014**, *53*, 225–227. Available online: <https://hrcak.srce.hr/110268> (accessed on 1 April 2014).
38. Liu, Q.L.; Li, X.M.; Jiang, Y.H. Numerical simulation of EBCHM for the large-scale Ti–6WT%AL–4WT%V alloy slab ingot during the solidification process. *Vacuum* **2017**, *141*, 1–9. [CrossRef]
39. Okabe, T.; Schulzrinne, H. Peer-to-Peer SIP features to eliminate a SIP sign-up process. In Proceedings of the IEEE GLOBECOM 2008—2008 IEEE Global Telecommunications Conference, New Orleans, LA, USA, 2008, 30 November–4 December; IEEE: New York, NY, USA, 2008; pp. 1–5. [CrossRef]

**Disclaimer/Publisher’s Note:** The statements, opinions and data contained in all publications are solely those of the individual author(s) and contributor(s) and not of MDPI and/or the editor(s). MDPI and/or the editor(s) disclaim responsibility for any injury to people or property resulting from any ideas, methods, instructions or products referred to in the content.